CROSS-FLOW STEREO PIV MEASUREMENTS IN WALL TURBULENCE

J. M. Barros and K. T. Christensen
Department of Mechanical Science and Engineering
University of Illinois
Urbana, IL 61801 USA
ktc@illinois.edu

ABSTRACT

Wide field of view stereo PIV measurements were conducted in the wall-normal–spanwise plane of fully-developed turbulent channel flow. These experiments represent a significant challenge to the stereo PIV method as the dominant velocity component was oriented normal to the PIV measurement plane while the in-plane components were predominantly much weaker turbulent fluctuations. Nevertheless, these measurements agreed well with DNS results at a similar Reynolds number, both in the mean streamwise velocity as well as the Reynolds normal and shear stresses, which validated the experimental methodology employed. Inspection of instantaneous velocity fields in this cross plane uncovered the spatial signatures of low- and high-momentum regions, the former of which have been previously linked to hairpin vortex packets in the outer layer of wall turbulence. POD was employed to study the spatial characteristics of the large-scale motions further and revealed a significant spanwise coherence in the form of alternating low- and high-momentum regions well beyond that reflected in two-point velocity correlations.

INTRODUCTION

The spatial characteristics of large-scale motions in wall turbulence have been the subject of intense study, particularly with recent evidence suggesting that the larger scales modulate the smaller-scale motions in the near-wall region (Mathis *et al.*, 2009). The streamwise–wall-normal ($x-y$) plane two-dimensional PIV measurements of Adrian *et al.* (2000*b*) provided a direct visualization of the coherent ordering of hairpin-like structures into larger-scale structural entities termed hairpin vortex packets. In particular, the streamwise alignment of individual hairpin-like structures into larger-scale packets observed by Adrian *et al.* (2000*b*) across the boundary layer in a hierarchy of scales is marked by an inclined interface formed by the spanwise-oriented heads of each structure beneath which a region of streamwise momentum deficit is apparent due to the collectively-induced ejection events generated by each of the vortices in a packet. Thus, these large-scale packets induce low-momentum regions (LMRs) previously identified in streamwise–spanwise plane PIV measurements that are bounded by wall-normal vortex cores likely associated with the legs/necks of the individual vortices of hairpin packets (Ganapathisubramani *et al.*, 2003; Tomkins & Adrian, 2003; Wu & Christensen, 2010) and within which intense ejections of low-speed fluid occur (Ganapathisubramani *et al.*, 2003; Wu & Christensen, 2010). Instantaneous PIV fields in the $x-z$ plane within the log layer also reveal the existence of high-momentum regions (HMRs) adjacent to LMRs within which strong sweep events are observed. This spanwise-alternating behavior of LMRs and HMRs is consistent with the spanwise-alternating sign of the two-point correlation of streamwise velocity in the $x-z$ plane (Ganapathisubramani *et al.*, 2005; Wu & Christensen, 2010). More recently, hot-wire experiments indicate that the LMRs observed in δ-scale PIV studies can actually extend several δ in the streamwise direction (Hutchins & Marusic, 2007). These 'superstructures' can meander significantly in the spanwise direction (Hutchins & Marusic, 2007) and can embody a significant fraction of the turbulent kinetic energy and Reynolds shear stress (Kim & Adrian, 1999, for example). It is these motions that appear to amplitude modulate the smaller scales in the near-wall region of flow (Mathis *et al.*, 2009).

While providing significant information about the structural characteristics of the flow, measurements at fixed wall-normal locations (or equivalently in fixed $x-z$ PIV planes) unfortunately do not provide details as to the wall-normal dependence of the spanwise scales of motion. Measurements in the wall-normal–spanwise ($y-z$) plane overcome such limitations; however, measurements in this cross-flow plane are extremely challenging as the bulk flow direction is normal to the PIV lasersheet. Nevertheless, a few studies have successfully employed PIV to study wall turbulence in the cross-flow plane (Ganapathisubramani *et al.*, 2005; Hutchins *et al.*, 2005; Carlier & Stanislas, 2005). In particular, Hutchins *et al.* (2005) and Ganapathisubramani *et al.* (2005) used stereo PIV in cross-flow planes inclined at 45° and 135° to the streamwise direction in a replication of the original flow-visualization imaging planes of Head & Bandyopadhyay (1981). These measurements revealed inclined vortical structures bounding LMRs that are consistent with the hairpin vortex packet model of wall turbulence. Spanwise-adjacent HMRs were also observed in the instantaneous fields,

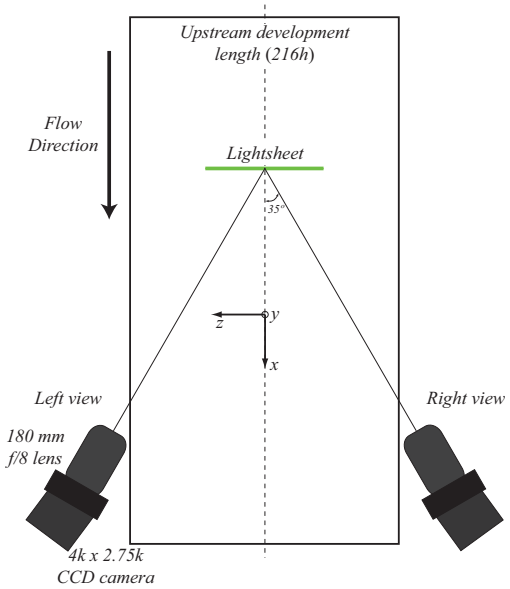

Figure 1. Schematic of the stereo PIV arrangement.

with both LMR and HMR events extending well into the outer layer of the flow. Analysis of spatial correlations of velocity in these inclined cross-flow planes also uncovered imprints consistent with hairpin vortex packets. However, the spanwise extent of these studies did not capture more than pairs of LMRs and HMRs in the spanwise direction, and so any spanwise ordering beyond that reflected in these limited spanwise views could not be assessed.

The present contribution concerns wide field of view cross-flow stereo PIV measurements in turbulent channel flow to study the spanwise coherence of large-scale motions. Two-point correlations are employed to study this coherence in the original fluctuating velocity fields as well as in fluctuating fields low-pass-filtered via proper orthogonal decomposition wherein only the larger spatial scales were preserved.

EXPERIMENT

The channel-flow facility used in this work has a development length of $216h$, where $h = 25.4$ mm is the half-height of the channel. The aspect ratio of the flow cross-section is 10.125:1, yielding nominally two-dimensional flow along the channel's spanwise centerline. The working fluid was air and the flow was conditioned upstream of the channel by a series of screens, honeycomb and a contraction. At the channel entrance, the flow on the top and bottom walls was tripped by 36-grid sandpaper, ensuring fully-developed flow conditions at the measurement section. In order to evaluate the wall shear stress, τ_w, static pressure readings were taken along the development length of the channel. Density and viscosity were assessed by measuring the fluid temperature and atmospheric pressure and employing an ideal gas relation in addition to Sutherland's correlation for kinematic viscosity. Using these fluid properties, the friction velocity, $u_\tau \equiv (\tau_w/\rho)^{1/2}$ and the viscous length scale, $y^* \equiv \nu/u_\tau$, were determined. Measurements were conducted for fully-developed flow at $\mathrm{Re}_\tau = 600$ with $u_\tau = 0.37$ m/s and $y_* = 41.4\,\mu$m.

Stereo PIV was used to measure all three velocity components in the wall-normal–spanwise $(y-z)$ plane of the flow in the fully-developed regime. The system employed consisted of two 4k $\times$ 2.75k pixel, 12-bit, frame-straddle CCD cameras (TSI 11MP) and a 190 mJ/pulse dual-cavity pulsed Nd:YAG laser (Quantel). A 1.0 mm thick laser lightsheet was formed by three cylindrical lenses and directed into the channel test section in the $y-z$ plane from above across the spanwise center of the tunnel. Figure 1 presents a schematic of the stereo PIV arrangement. The cameras viewed the $y-z$-oriented lightsheet from downstream through optical-grade glass side-walls of the channel at angles of $\pm 35^\circ$ from the streamwise (x) direction. Lenses with a fixed focal length of 180 mm were utilized to image a field of view of approximately $4h \times h$ (spanwise by wall-normal) with an f-number of 8. The angle between each lens and camera CCD array was adjusted to satisfy the Scheimpflug condition which ensured uniform focus across the field of view. The flow was seeded with 1 μm olive-oil droplets generated by a Laskin nozzle and timing of the cameras, lasers and image acquisition was controlled with a timing unit with 1 ns resolution.

Accurate stereo PIV measurements required careful calibration of the imaging system to properly map the image coordinate system to the object plane defined by the laser lightsheet. A target consisting of dots spaced at 2 mm in both the horizontal and vertical directions was carefully aligned to be coincident with the laser lightsheet. Images of this target were then acquired by both cameras at this position as well as with the target translated $\pm 500\,\mu$m upstream and downstream of lightsheet center. Using images of the target at multiple depths, a calibration mapping function was generated to map the two, 2-D image planes to the 3-D space defined by the laser lightsheet using the least-squares method of Soloff *et al.* (1997). Thus, the out-of-plane fluid motion was discerned from the distinct views of the tracer-particle motion within the laser lightsheet as imaged by the two cameras.

Two-thousand five-hundred statistically-independent planar, three-component velocity fields were acquired. As mentioned above, each three-component velocity field was derived from two, 2D displacement fields generated from the time-delayed pairs of images acquired by each camera. These pairs of time-delayed images were interrogated using a recursive, two-frame cross-correlation methodology. The first-pass interrogation was performed with a bulk window offset to minimize loss of particle pairs while the final-pass interrogation was performed with square interrogation spots of size 16^2 pixels with 50% overlap to satisfy the Nyquist sampling criterion and the second window was locally offset by an integer displacement determined during the first-pass interrogation. Statistical validation tools were employed between passes to identify and replace erroneous vectors as well as after the final interrogation pass was completed, including Rohaly–Hart replacement with displacements assessed from alternate correlation peaks identified during the interrogation process (Rohaly *et al.*, 2002). All fields were also low-pass filtered with a narrow Gaussian filter to remove high-frequency noise. Each pair of 2-D displacement fields was then recombined using the aforementioned mapping function to reconcile all three instantaneous velocity components on the measurement plane defined by the laser lightsheet with an in-plane grid spacing of 237 μm in the wall-normal and spanwise directions. This grid spacing

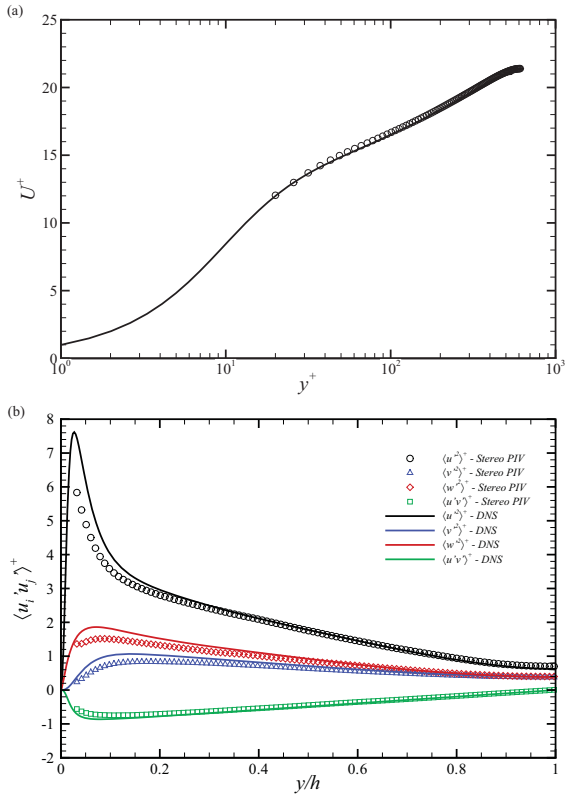

Figure 2. (a) Inner-scaled mean velocity profile and (b) Reynolds stresses compared with DNS results (Moser *et al.*, 1999).

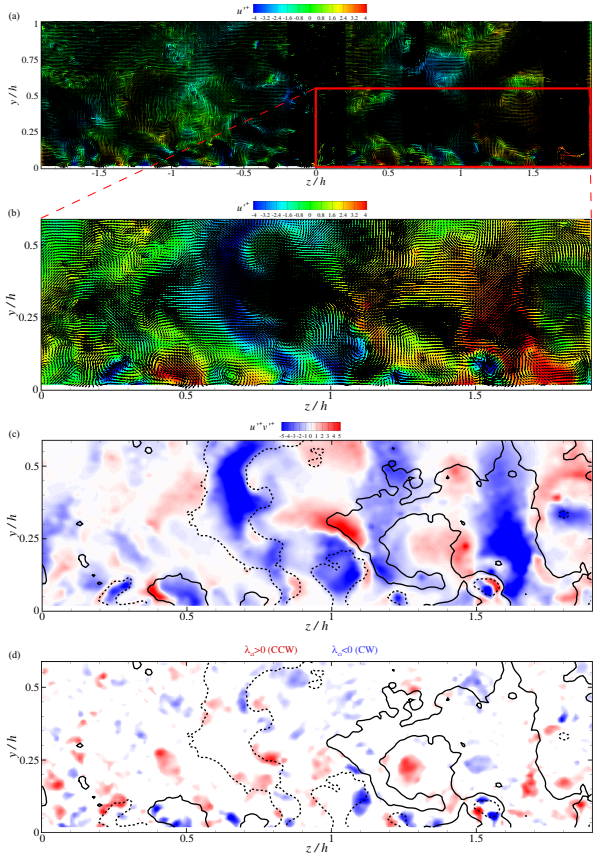

Figure 3. Representative instantaneous fluctuating velocity field in the $y-z$ plane. (a) Full field; (b) Zoomed-in view coincident with red-bordered box in (a); Contours of (c) instantaneous Reynolds shear stress, $u'v'$, and (d) signed swirling strength, λ_{ci}, for zoomed-in view in (b). Solid and dashed line contours in (c) and (d) demarcate boundaries of HMRs and LMRs, respectively.

translates into a spatial resolution of $11.2y_*$. The stereo reconstruction yielded a 406×107 vector grid of instantaneous velocity vectors on the $4h \times h$ field of view.

RESULTS

Single-point statistics were computed from the ensemble of 2500 velocity fields by ensemble averaging followed by line-averaging in the statistically-homogeneous spanwise direction. Thus, each data point represents an average over 812,000 velocity samples. The sampling error is estimated to be less than 1%, though the uncertainty of these statistics when scaled in inner units (i.e., by u_τ and ν) is approximately 4% due to the uncertainty in estimating u_τ via measurements of the streamwise pressure gradient and fluid properties. Thus, symbol size embodies the uncertainty bounds for each statistic presented.

Figure 2(a) presents the inner-scaled mean velocity profile (U^+ versus y^+) for the smooth-wall case compared with the result from a direct numerical simulation (DNS) at $\mathrm{Re}\tau = 550$ (Moser *et al.*, 1999). While the experimental data does not resolve the viscous sublayer nor most of the buffer layer, as the first grid-point resides at $y^+ = 17.6$ ($y = 0.0293h$), the expected log-layer behavior is observed as the experimental result is in good agreement with the DNS profile. Figure 2(b) presents profiles of all three Reynolds normal stresses ($\langle u'^2 \rangle$, $\langle v'^2 \rangle$ and $\langle w'^2 \rangle$) as well as the Reynolds shear stress ($\langle u'v' \rangle$) compared to the same profiles garnered from DNS (Moser *et al.*, 1999). This comparison reveals a reasonable level of agreement between the experimental and computational results, including in the Reynolds shear stress where both profiles exhibit the characteristic linear behavior in the outer region due to the dominance of turbulent stresses over viscous stresses. Some differences are noted in the near-wall region where all three Reynolds normal stresses are slightly underestimated compared to their DNS counterparts. These differences are partially due to the finite size of the interrogation windows employed when interrogating the PIV images which necessarily yields averaging over structures smaller than this dimension. In addition, as the wall is approached the relative error in the velocity fluctuations increases owing to a fixed resolvable particle displacement (~ 0.1 pixels) coupled with a reduction in the mean streamwise velocity compared to the outer region of the flow. Nevertheless, the consistency of these turbulent stresses with the DNS result to within roughly 10% ($\pm 4\%$ due to uncertainty in u_τ) is encouraging, particularly since our present interest is in the behavior of the larger spatial scales of the flow.

Figure 3(a) presents a representative instantaneous fluctuating velocity field in the wall-normal–spanwise ($y-z$) plane of turbulent channel flow at $\mathrm{Re}_\tau = 600$. The in-plane

wall-normal (v') and spanwise (w') velocity fluctuations are shown as vectors while the out-of-plane streamwise velocity fluctuations (u') are presented as background contours. The streamwise velocity fluctuations are marked by large-scale (h-scale) regions of low and high streamwise momentum that appear to alternate in the spanwise direction. These regions, which can extend to, or even beyond, the channel centerline represent the cross-plane signatures of LMRs and HMRs that have been previously identified in wall-parallel PIV measurements (Ganapathisubramani *et al.*, 2003; Tomkins & Adrian, 2003; Wu & Christensen, 2010) and most recently linked to superstructures that can extend several outer length scales in the streamwise direction while meandering in the spanwise direction (Hutchins & Marusic, 2007). Figure 3(b) presents a zoomed-in view of a portion of the full field in figure 3(a) [demarcated by the red box] in which a large-scale LMR and a large-scale HMR are notable and separated in the spanwise direction by $\sim 0.5h$. Both of these large-scale events extend well into the outer layer ($y \approx 0.5-0.75h$). Focusing upon the visualized LMR in figure 3(b), which have been previously linked to the low-momentum regions collectively induced by the vortices within hairpin packets, streamwise vortices are notable along its left and right boundaries. In addition, this LMR embodies significant instantaneous contributions of Reynolds shear stress as is apparent in figure 3(c) which presents contours of instantaneous $u'v'$ overlaid with line contours of $u'^{+} = \pm 2$ meant to outline the boundaries of the various LMRs and HMRs present in this realization. In particular, the positive v' noted within this LMR coupled with the negative u', characteristic of an LMR, together yield a large-scale region of negative $u'v'$ associated with ejection of low-speed fluid away from the wall. This observation is again consistent with the hairpin packet model. Likewise, the negative v' noted within the visualized HMR in figure 3(b) coupled with the positive u', characteristic of an HMR, yields a region of negative $u'v'$ that is due to the sweeping of high-speed fluid from the outer region toward the wall. Apart from these h-scale events, smaller LMRs and HMRs are visualized in the near-wall region that are often bounded by vortical structures. These smaller-scale regions appear to coexist beneath the larger-scale LMRs and HMRs, supporting the notion that such structures occur in a hierarchy of scales across the flow. As proposed by Adrian *et al.* (2000*b*), packets of varying size would be expected throughout the wall-normal extent of the flow, with smaller, younger, slower packets residing closer to the wall where they are likely formed and successively larger, older packets populating the outer region of the flow while maintaining a near-wall footprint. Finally, figure 3(d) presents contours of swirling strength, a local vortex identifier (Adrian *et al.*, 2000*a*), marked with the sign of the instantaneous streamwise vorticity to distinguish between clockwise- and counter-clockwise-rotating vortices in the $y-z$ plane (line contours of $u'^{+} = \pm 2$ demarcating the boundaries of the LMRs and HMRs are also included). A few counter-rotating pairs of streamwise vortex cores are notable outboard of the LMRs and HMRs, with the former consistent with slices through the legs/necks of hairpin-like structures that collectively induce ejections of low-speed fluid away from the wall. However, most of the streamwise vortex cores visualized in figure 3(d) seem to occur in isolation, consistent with previous observations that many hairpin-like structures are asymmetric in nature (Zhou *et al.*, 1999).

Figure 4(a)–(d) presents two-point velocity correlation coefficients in the $y-z$ measurement plane defined as

$$\rho_{ij}(y,\Delta z;y_{\mathrm{ref}}) = \frac{\langle u_i'(y_{\mathrm{ref}},z)u_j'(y,z+\Delta z)\rangle}{\sigma_i(y_{\mathrm{ref}})\sigma_j(y)}, \qquad (1)$$

specifically ρ_{uu}, ρ_{vv}, ρ_{ww} and ρ_{uv}, respectively, at $y_{\mathrm{ref}} = 0.15h$. Here, u_i' is the i^{th} velocity fluctuation ($i,j = 1,2,3$), σ_i is the root-mean-square of u_i' and Δz is the offset in the spanwise direction. These correlations were computed by averaging over all 2500 fluctuating velocity fields. As has been reported in previous studies, particularly from PIV measurements in the $x-z$ plane of wall turbulence (Tomkins & Adrian, 2003; Ganapathisubramani *et al.*, 2003; Wu & Christensen, 2010), ρ_{uu} is marked by a primary peak at $(y,z) = (y_{\mathrm{ref}} = 0.15h, 0)$ that is bounded by correlation minima in the spanwise direction. This alternating pattern is consistent with the occurrence of spanwise-alternating LMRs and HMRs as supported by the instantaneous realization of figure 3. Interestingly, these regions of high and low correlation extend from the near-wall region to the centerline of the channel, indicating that they are attributable to large-scale (h-scale) features of the flow. In contrast, ρ_{vv} is smaller in spanwise scale, though it is still characterized by a primary correlation peak at $(y,z) = (y_{\mathrm{ref}} = 0.15h, 0)$ that is bounded by correlation minima in the spanwise direction. This pattern is consistent with the imprint of streamwise vortices pumping low-speed fluid away from the wall and drawing high-speed fluid toward the wall. Similar behavior is noted in ρ_{uv}. Interestingly, all of these velocity correlations show correlation patterns of alternating sign with increasing spanwise separation, albeit extremely weak in magnitude (though still above the sampling error at these large separations).

To further explore the large-scale characteristics of the flow in the $y-z$ plane, proper orthogonal decomposition (POD) was employed. This technique is particularly well-suited for systems that are statistically inhomogeneous in one or more spatial directions, wherein complex infinite-dimensional processes can be represented using lower-dimensional approximate descriptions. In particular, POD generates a basis for the modal decomposition of the instantaneous fluctuating velocity fields and provides the most efficient way of identifying the motions which, on average, contain a majority of the turbulent kinetic energy (TKE) in the flow (Holmes *et al.*, 1996). In this regard, the lowest-order (most energetic) modes typically embody the larger spatial scales of the flow while the higher-order (less energetic) modes represent increasingly smaller spatial scales. The snapshot POD method was utilized herein to compute the POD modes and associated eigenvalues in the $y-z$ plane as it is more amenable to the discrete nature of PIV velocity fields.

Of interest in the present effort was utilizing the lower-order POD modes as a low-pass filter to separate the large and small scales in the instantaneous fluctuating velocity fields. This filtering was accomplished by projecting each fluctuating velocity field onto the first 10 most energetic POD modes (embodying about 25% of the TKE in the $y-z$ plane), meaning the smaller spatial scales in the fields were truncated while the larger, more energetic scales were preserved (Wu & Christensen, 2010). Figure 5 presents the result of this low-order reconstruction methodology applied to the instantaneous ve-

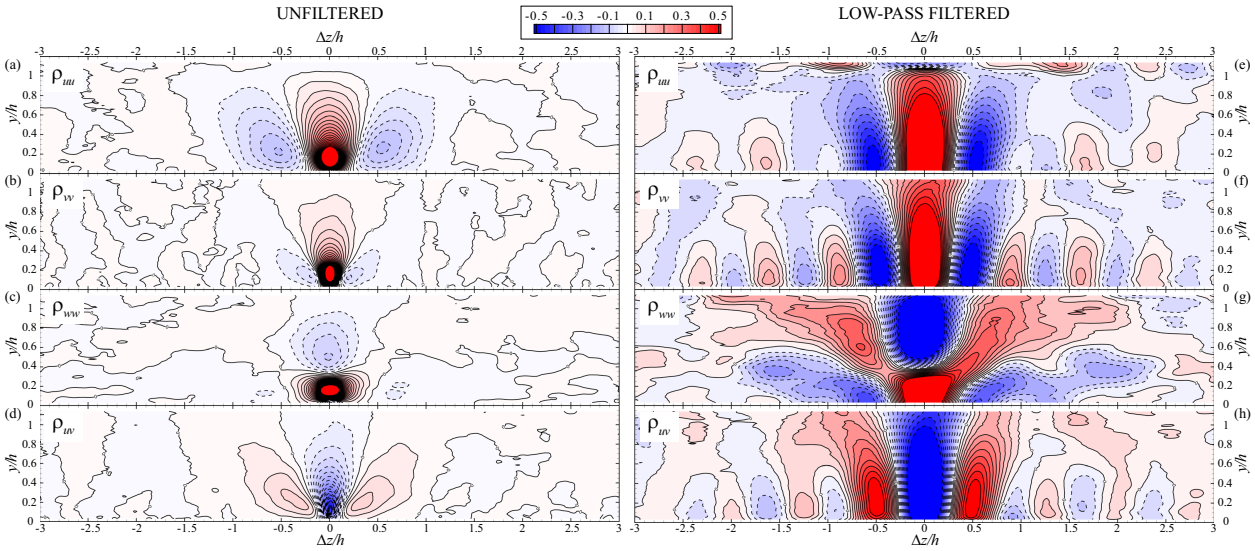

Figure 4. Two-point velocity correlation coefficients in the $y-z$ plane computed from (a)–(d) original fluctuating fields and (e)–(h) low-pass-filtered fluctuating velocity fields via projection onto first 10 POD modes.

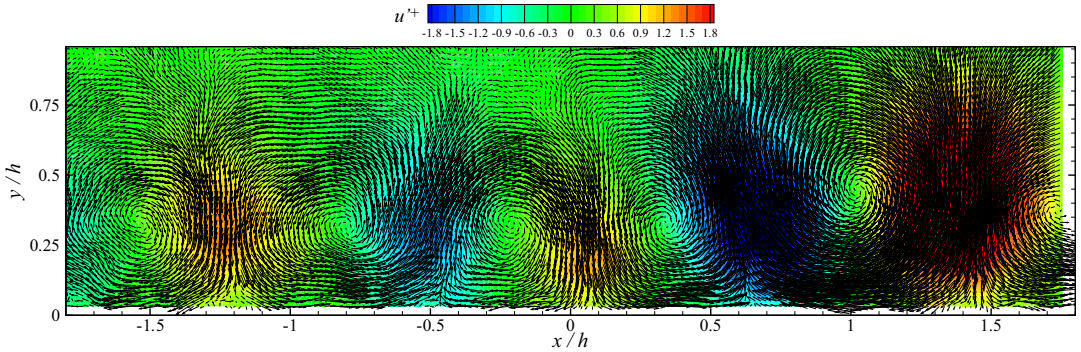

Figure 5. Large-scale reconstruction of instantaneous velocity field presented in figure 3(a) using the first 10 POD modes. In-plane velocities presented as vectors and out-of-plane velocity shown as contours.

locity field in figure 3(a). This field is clearly a low-pass-filtered version of the original fluctuating field as only the larger-scale features of the field are retained. Despite truncation of the smaller scales, there still exists strong visual similarities between the original field and the low-order reconstruction, particularly the spanwise-alternating regions of low and high streamwise momentum. These LMRs and HMRs have a spanwise extent of $\sim 0.5h$ and a spanwise spacing of $\sim 0.5-0.75h$, consistent with the overall characteristics of ρ_{uu} in figure 4(a). Interestingly, the boundaries between these alternating LMRs and HMRs are marked by streamwise vortices that drive low-speed fluid away from the wall in the case of the LMRs and draw high-speed fluid toward the wall in the case of the HMRs.

While the spanwise-alternating LMRs and HMRs evident in the low-order reconstruction of a representative instantaneous velocity field in figure 5 is consistent with the overall character of ρ_{uu} [figure 4(a)], the alternating nature of LMRs and HMRs in this example extends well beyond simply a single LMR bounded on either spanwise side by an HMR (or vice-versa) as implied by ρ_{uu}. Rather, this low-order reconstruction indicates that an even more ordered arrangement of these large-scale motions may exist in the spanwise direction that is not necessarily reflected in the two-point correlations [figure 4(a)–(d)], possibly because of smaller-scale variability in the flow. To explore this possibility, all 2500 instantaneous velocity fields were projected onto the first 10 modes derived from the snapshot POD analysis, yielding an ensemble of 2500 instantaneous, low-pass-filtered velocity fields embodying only the larger-scale motions of the flow. This ensemble of low-pass-filtered fields was then used to compute two-point correlation coefficients as described by eqn. (1) at $y_{\mathrm{ref}} = 0.15h$ [figure 4(e)–(h)] that reflect the spatial coherence of only the large-scale motions in the $y-z$ plane. Strikingly consistent with the overall character of the instantaneous low-pass-filtered velocity field in figure 5, the correlation ρ_{uu} supports a spanwise-alternating ordering of LMRs and HMRs well beyond that indicated by the original, unfiltered version of ρ_{uu} in figure 4(a). In particular, the correlation minima outboard of the primary correlation peak in ρ_{uu} are flanked by localized maxima that are then flanked outboard again by localized minima. This spanwise-alternating character of the large scales extends $4h$ in the spanwise direction. A similar spanwise ordering is also evident in both ρ_{vv} and ρ_{uv} computed from the low-pass-filtered fluctuating velocity ensemble.

Finally, the overall statistical imprint of the large scales

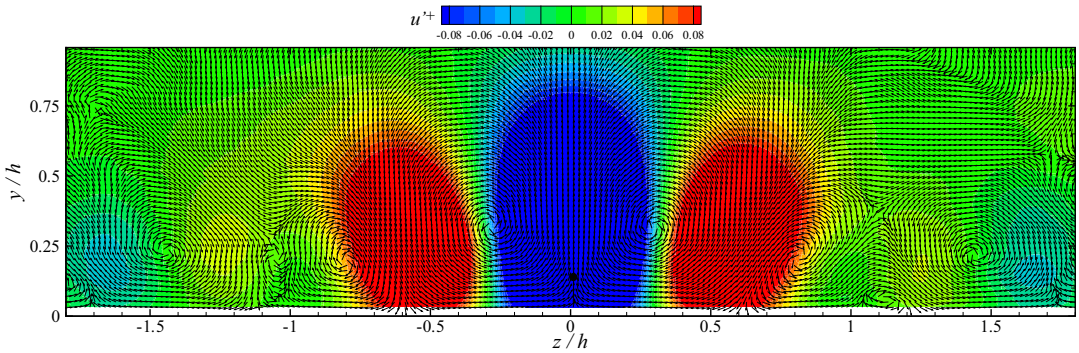

Figure 6. Estimate of the conditional low-pass-filtered velocity field given an LMR at $(y,z) = (y_{\text{ref}} = 0.15h, 0)$. In-plane velocities presented as unit vectors and out-of-plane velocity shown as contours. Event location demarcated by •.

in the $y-z$ plane was explored by estimating the conditional fluctuating velocity field associated with an LMR in the low-pass-filtered velocity fields, $\langle u_i'(y,z)|u'(y_{\text{ref}} = 0.15h, 0) < 0\rangle$, via linear stochastic estimation. This result is presented in figure 6 with the in-plane velocities shown as vectors of unit length (denoting direction) and the streamwise (out-of-plane) velocity presented as contours. This estimate of the conditional velocity field associated with an LMR bears a striking resemblance to the instantaneous low-pass-filtered velocity field in figure 5, particularly the spanwise-alternating nature of the LMRs and HMRs across the entire spanwise field of view ($\sim 4h$) and the occurrence of streamwise vortices between adjacent LMRs and HMRs. For reference, estimates of the same conditional velocity field given an LMR from the original, unfiltered fluctuating velocity fields (not shown) embodies only a single LMR bounded on either side by HMRs. Thus, the spatial ordering of the large scales appears masked by the smaller-scale variability in the flow and was only revealed via scale separation, herein accomplished with POD.

SUMMARY

The wide field of view stereo PIV measurements in the $y-z$ plane presented herein revealed a distinct spanwise ordering of LMRs and HMRs well beyond that reflected in two-point correlations of velocity. The relationship between this large-scale ordering and the smaller scales of the flow is currently under investigation. In addition, the nature of this behavior at higher Re as well as in the presence of roughness in a turbulent boundary layer is under study.

ACKNOWLEDGEMENTS

This work was supported by the Air Force Office of Scientific Research (Dr. John Schmisseur, Program Manager).

REFERENCES

Adrian, R. J., Christensen, K. T. & Liu, Z.-C. 2000*a* Analysis and interpretation of instantaneous turbulent velocity fields. *Exp. Fluids* **29**, 275–290.

Adrian, R. J., Meinhart, C. D. & Tomkins, C. D. 2000*b* Vortex organization in the outer region of the turbulent boundary layer. *J. Fluid Mech.* **422**, 1–54.

Carlier, J. & Stanislas, M. 2005 Experimental study of eddy structures in a turbulent boundary layer using particle image velocimetry. *J. Fluid Mech.* **535**, 143–188.

Ganapathisubramani, B., Hutchins, N., Hambleton, W. T., Longmire, E. K. & Marusic, I. 2005 Investigation of large-scale coherence in a turublent boundary layer using two-point correlations. *J. Fluid Mech.* **524**, 57–80.

Ganapathisubramani, B., Longmire, E. K. & Marusic, I. 2003 Characteristics of vortex packets in turbulent boundary layers. *J. Fluid Mech.* **478**, 35–46.

Head, M. R. & Bandyopadhyay, P. 1981 New aspects of turbulent boundary-layer structure. *J. Fluid Mech.* **107**, 297–338.

Holmes, P., Lumley, J. L. & Berkooz, G. 1996 *Turbulence, Coherent Structures, Dynamical Systems and Symmetry*. Cambridge University Press.

Hutchins, N., Hambleton, W. T. & Marusic, I. 2005 Inclined cross-stream stereo particle image velocimetry measurements in turbulent boundary layers. *J. Fluid Mech.* **541**, 21–54.

Hutchins, N. & Marusic, I. 2007 Evidence of very long meandering features in the logarithmic region of turbulent boundary layers. *J. Fluid Mech.* **579**, 1–28.

Kim, K. C. & Adrian, R. J. 1999 Very large-scale motion in the outer layer. *Phys. Fluids* **11**, 417–422.

Mathis, R., Hutchins, N. & Marusic, I. 2009 Large-scale amplitude modulation of the small-scale structures in turbulent boundary layers. *J. Fluid Mech.* **628**, 311–337.

Moser, R. D., Kim, J. & Mansour, N. N. 1999 Direct numerical simulation of turbulent channel flow up to Re_τ = 590. *Phys. Fluids* **11** (4), 943–945.

Rohaly, J., Frigerio, F. & Hart, D. 2002 Reverse hierarchical piv processing. *Meas. Sci. Technol.* **13**, 984–996.

Soloff, S. M, Adrian, R. J. & Liu, Z-C 1997 Distortion compensation for generalized stereoscopic particle image velocimetry. *Meas. Sci. Technol.* **8** (1441-1454).

Tomkins, C. D. & Adrian, R. J. 2003 Spanwise structure and scale growth in turbulent boundary layers. *J. Fluid Mech.* **490**, 37–74.

Wu, Y. & Christensen, K. T. 2010 Spatial structure of a turbulent boundary layer with irregular surface roughness. *J. Fluid Mech.* **455**, 380–418.

Zhou, J., Adrian, R. J., Balachandar, S. & Kendall, T. M. 1999 Mechanisms for generating coherent packets of hairpin vortices in channel flow. *J. Fluid Mech.* **387**, 353–396.